

Origami spring-inspired shape morphing for flexible robotics

Qianying Chen^{1,2}, Fan Feng¹, Pengyu Lv¹, and Huiling Duan^{1,2*}

¹State Key Laboratory for Turbulence and Complex Systems, Department of Mechanics and Engineering Science, BIC-ESAT, College of Engineering, Peking University, 100871 Beijing, China

²CAPT, HEDPS and IFSA Collaborative Innovation Center of MoE, Peking University, 100871 Beijing, China

*Correspondence and requests for materials should be addressed to H.D.(email:hlduan@pku.edu.cn)

ABSTRACT

Flexible robotics are capable of achieving various functionalities by shape morphing, benefiting from their compliant bodies and reconfigurable structures. Here we construct and study a class of origami springs generalized from the known interleaved origami spring, as promising candidates for shape morphing in flexible robotics. These springs are found to exhibit nonlinear stretch-twist coupling and linear/nonlinear mechanical response in the compression/tension region, analyzed by the demonstrated continuum mechanics models, experiments, and finite element simulations. To improve the mechanical performance such as the damage resistance, we establish an origami rigidization method by adding additional creases to the spring system. Guided by the theoretical framework, we experimentally realize three types of flexible robotics – origami spring ejectors, crawlers, and a transformer, which show the desired functionality and outstanding mechanical performance. The proposed concept of origami-aided design is expected to pave the way to facilitate diverse shape morphing of flexible robotics.

Keywords: shape morphing, origami springs, structural design, flexible robotics.

1 Introduction

Flexible robotics possess compliant bodies and reconfigurable structures so as to achieve multiple functionalities, such as grabbing or releasing objects of different materials^{1,2}, and crawling or swimming in diverse environments^{3,4}. The essential performance of flexible robotics for functionality is the controllable shape morphing, based on materials or structural design or both. The material-based shape morphing, which can be classified into two categories according to the characteristics of deformation: soft-material-based robots with passive shape-morphing ability and smart-material-based robots with active shape-morphing ability. The emphasis of the former is to seek efficient and convenient actuation strategies like pneumatic, hydraulic, or chemical energy to drive the shape change of robots^{1,4,5}, while the latter is to explore advanced smart materials including shape memory alloys and optical-/magnetic-/thermal-response materials to realize specific deformations in response to the external stimuli^{6–13}.

Shape-morphing strategies based on structural design are focused on exploiting special structures with specific mechanical properties, such as negative Poisson's ratio^{14,15}, multistability^{16–18}, and buckling¹⁹ for flexible robotics. Moreover, structural shape morphing can provide various and programmable deformation modes rather than simple swelling or shrinkage, and thus have many advantages and great

potential prospects²⁰. Among various structural design strategies, origami made of thin paper ribbon is a promising candidate^{2,21–25}, benefiting from its inherent structural and mechanical properties. First, origami is constructed by folding the paper along the prescribed creases on an easy-to-manufacture two dimensional sheet. The distribution of creases can be designed to provide desired geometrical constraints, leading to different degrees of freedom of motion and potentially simple control systems^{23,26–28}. Second, the bending effect usually dominates in the origami system, introducing generically nonlinear effective mechanical response, which can be utilized to design origami springs^{24,26,29}, origami cantilevers^{30,31}, etc. Despite having various designs of origami actuators/robotics in the literature, these applications usually suffer from one of the difficulties or the other: 1. The models to capture the shape morphing rules and the mechanical response are usually sophisticated, which enhance the difficulties of the shape-morphing analysis when we integrate origami into flexible robotics as compound structures; 2. There usually exists inevitable stress concentration to the extent at the corner of the creases, especially in flexible origami, which results in undesired damage to the structures. Therefore, it is necessary to develop new theoretical methods to overcome these difficulties and guide the further use of origami in flexible robotics.

In this work, we consider the generalized origami springs as a template for the application of flexible robotics which also overcome the above-mentioned difficulties to some extent. To this end, we firstly introduce a series of origami springs by alternately folding multiple regular-polygon-array paper ribbons, which is a generalization of the known interleaved origami spring (IOS). IOSs exhibit stretch-twist-coupling shape morphing benefited from the mutual deformation restraints and interactions among the interleaved paper ribbons. We demonstrate a continuum mechanics model to simplify the analysis of the shape morphing and the mechanical response of IOS. The theoretical model is validated by the experiments and finite element simulations. Moreover, to optimize the mechanical response and improve the damage resistance, we propose an origami rigidization method by predesigning additional creases on the facets to guide the shape-morphing trends. The simulation shows that the origami rigidization significantly lowers the stress concentration and enhances the damage resistance of the structure. Then, the theoretically, experimentally, and numerically analyzed shape-morphing performances and mechanical response of IOSs are further applied to construct flexible robotics, including the origami spring ejectors, crawlers, and a transformer, which demonstrate the feasibility of the origami-aided-design concept. Finally, we anticipate that the design framework can be generalized and applied to other systems such as stimuli-sensitive and non-periodic origami.

2 Results

2.1 Construction of the origami spring.

The zigzag origami (ZO) is the simplest origami structure to provide elasticity of a rectangular paper ribbon through the alternate mountain-valley folding, whose elastic performance is related to the property of crease. Applying the uniaxial force F , the ZO behaves as a nonlinear spring with no twist involved (see Fig. 1a). Inspired by the ZO, we construct an origami spring which is known as the interleaved origami spring (IOS) by alternately folding two perpendicularly arranged rectangular paper ribbons of the same

size (Fig. 1b). An IOS (or IOS-4) essentially consists of two interleaved ZO structures, therefore it also exhibits elasticity when stretched from the two ends. When subjected to a uniaxial force, in contrast with ZO, IOS shows a twist along the central axis (Fig. 1c) due to the interactions between these two paper ribbons. Besides the IOS, the stretch-twist coupling has also been observed in many other origami systems^{22,32,33} and found wide applications. To enrich the class of IOS, we also systematically fold ribbons consisting of chains of different shaped polygons (see Fig. 2 and Supplementary Section A). These IOSs are named as IOS-6, and IOS-8 respectively, depending on the shapes of the facets. IOS-6 is constructed by three paper ribbons consisting of a series of regular hexagons arrayed in chain. Before folding, three ribbons are placed in coincidence with the central axis 60 degrees apart, then are folded alternately in a similar way as IOS-4. Similarly, IOS-8 is constructed by four paper ribbons consisting of a series of regular octagon arrayed in chain with the central axis 45 degrees apart and folded in the same way (see Supplementary Figs. 7 and 8). They are expected to have distinct stretch-twist couplings and mechanical response due to the different interactions of facets, which will be analyzed later.

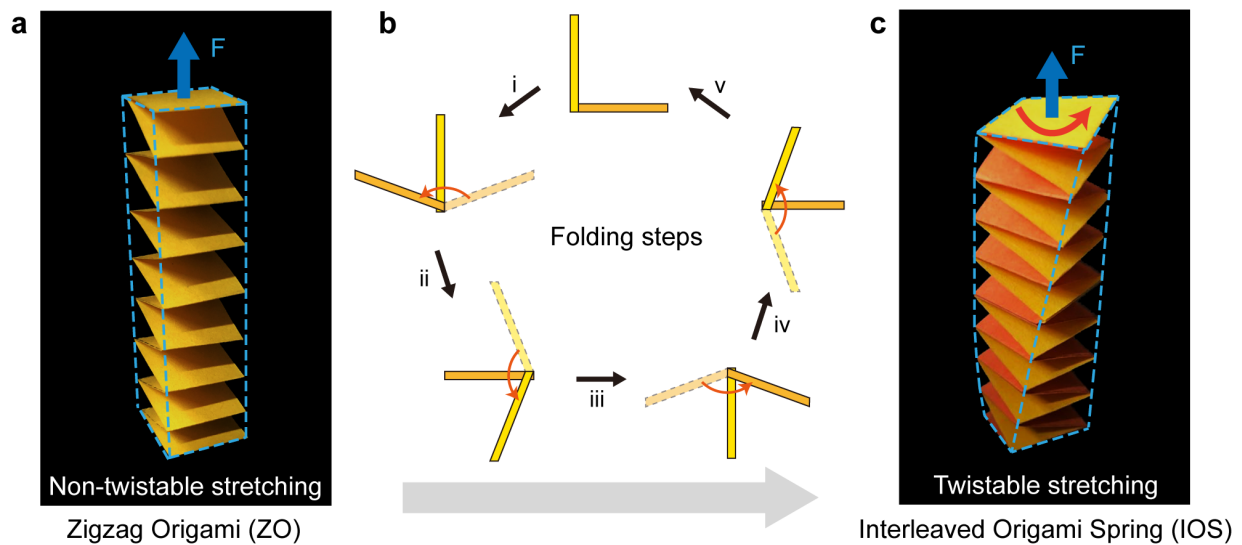


Fig. 1. Geometry of the zigzag origami (ZO) and interleaved origami spring (IOS). (a) The uniform-stretching configuration of ZO under uniaxial tension. (b) The folding process of IOS-4. (c) The stretch-twist-coupling shape morphing of IOS under uniaxial tension.

2.2 Shape morphing modeling.

In this section, we aim to analyze the shape morphing, specifically the stretch-twist coupling of IOSs, by replacing the origami structure with an analogous continuum having the same response. Fig. 2a shows the IOS-4 configurations and the corresponding analogous continuum diagrams in different extension ratios with eight unit cells. The continuum consists of a cylinder with four helices wound on the surface. According to the positions of origami vertices shown in Fig. 2a, three helices indicated by the solid blue

lines have large pitches, whereas one helix indicated by the dashed yellow line have a small pitch on the cylinder. During the stretch-twist shape morphing, three assumptions are satisfied in the simplified model. First, all the sides keep straight with a constant side length a ; second, the shape-morphing process is quasi-static, while all the unit cells keep the same configuration; third, all the origami vertices land on the small-pitch or large-pitch helices during the shape morphing process. The stretch-twist shape morphing performance is characterized by two dimensionless parameters, i.e., the twisting angle of each cell $\tilde{\theta}$, and the extension ratio \tilde{z} , which are defined as

$$\tilde{\theta} = \frac{\theta}{n}, \quad (1)$$

$$\tilde{z} = \frac{z}{l_{LPH}(a, n, z)} = \sin \varphi \quad (2)$$

where θ and z are the twisting angle and the extension length of the whole structure, respectively. n is the number of the unit cells, l_{LPH} is the arc length of the large-pitch helix, which is a function of a , n , and z , and φ is its helix angle.

We intercept four continuous facets of an IOS-4 as the shape-morphing unit cell, which consists of two square facets in each paper ribbon (Fig. 2b). Since point C and D trisect the curve of the small-pitch helix between point A and B , the z -axis coordinate of D can be approximately expressed by $z_D = z_A + a \sin \varphi / 3 = z_A + a \sin \varphi'$, implying $\varphi' = \arcsin(\tilde{z}/3)$, where z_A is the z -axis coordinate of A and φ' is the helix angle of the small-pitch one. Projecting the vertices of the unit cell onto the plane perpendicular to the cylindrical axis and passing through A , one can obtain the projected vertices B', \dots, G' (see Fig. 2b) and the sum of the projected arcs $\widehat{AB'} + \widehat{B'C'} + \widehat{C'D'} + \widehat{D'A} = 2\pi r$, where r is the radius of the cylinder. The expression of r is further deduced as a function of \tilde{z}

$$r = \frac{aN_8}{6} \sqrt{\frac{N_4(N_4 + M_4)}{6}}, \quad (3)$$

by calculating the projected arcs, where $M_4 = \sqrt{1 - \tilde{z}^2}$, $N_4 = \sqrt{9 - \tilde{z}^2}$. The twisting angle of each unit cell $\tilde{\theta}$ is also given as a function of \tilde{z}

$$\tilde{\theta}(\tilde{z}) = \frac{4(\widehat{E'B'} - \widehat{AB'})}{r} = 4 \arccos [P_4 Q_4 + \sqrt{1 - P_4^2} \sqrt{1 - Q_4^2}], \quad (4)$$

where $P_4 = 1 - 108M_4^2/[N_4^3(M_4 + N_4)]$, $Q_4 = 1 - 12/[N_4(M_4 + N_4)]$. Here the total twisting angle of a unit cell is the sum of the relative twisting angle between two adjacent facets $(\widehat{E'B'} - \widehat{AB'})/r$ (the unit cell contains four facets). The derivations of these functions can be found in Supplementary Section B.

We obtain the twisting angle θ and the corresponding extension length z through the finite element analysis (FEA) and experiments. $\tilde{\theta}$ and \tilde{z} can be further calculated by Eq. (1) and Eq. (4), respectively. The

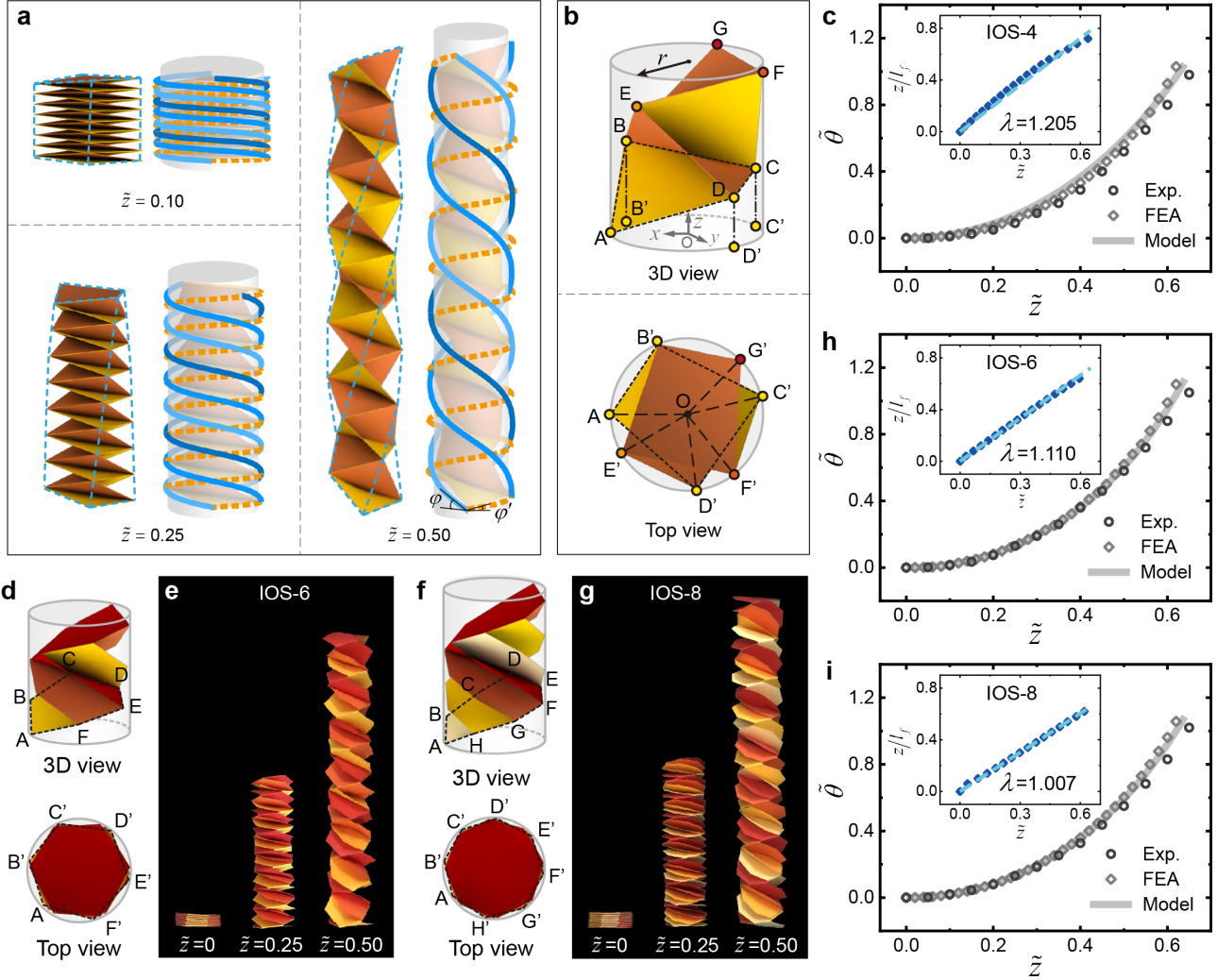


Fig. 2. Schematics of the stretch-twist-coupling performance of IOSs and continuum analysis diagrams. (a) The configurations of IOS-4 and the corresponding simplified equivalent continuum diagrams in extension ratio $\tilde{z} = 0.10, 0.25$, and 0.50 , respectively. Light-, sky-, and dark-blue solid lines indicate the large-pitch helices, while yellow dashed lines the small-pitch. (b) The shape-morphing model of the IOS-4 unit cell on 3D and top view, respectively. (c) The dependences of $\tilde{\theta}$ upon \tilde{z} for IOS-4. The data were obtained from experiments, FEA, and the proposed theoretical model. The thumbnail exhibits z/l_f as a function of \tilde{z} , showing an approximately linear relationship. (d-i) Similar analyses for IOS-6 and IOS-8. The results reveal the different stretch-twist couplings in IOS-4, IOS-6, and IOS-8.

relationship between z and \tilde{z} is approximately linear (Fig. 2c, inset), implying that l_{LPH} can be regarded as a constant independent of z . We thus assume

$$\tilde{z} = \frac{z}{\lambda l_f}, \lambda \geq 1, \quad (5)$$

where $\lambda l_f = l_{LPH}$, λ is a constant coefficient and $l_f (= 2an$ in IOS-4s) is the extension length of the IOS when $\varphi = \pi/2$. In Fig. 2c, the dependences of $\tilde{\theta}$ upon \tilde{z} (i.e., the stretch-twist coupling) from experiments, FEA, and our proposed model are plotted, which are in great agreements. Moreover, the $\tilde{\theta}(\tilde{z})$ curve shows a nonlinear (nearly quadratic) behavior, indicating the twisting speed increases as the length of the spring grows at a constant speed.

Similar analyses are also performed for IOS-6 and IOS-8. The geometric parameters of IOSs with different shaped facets but the same circumradius r_0 are listed in Supplementary Table 1 (derivation process see Supplementary Section B). The theoretical, FEA and experimental results in Figs. 2h and 2i reveal that similar stretch-twist couplings also exist in IOS-6 and IOS-8, with slight discrepancies. It is noted that λ tends to 1 when increasing the number of the regular-polygon edges, which means, as the number of the edges increases, the length of the large-pitch helix is close to the extension length when $\varphi = \pi/2$.

2.3 Structural optimization.

Inherently induced by the coupling of structure and material, the IOSs undergo more and more obvious buckling with the progress of stretching. Especially, stress concentrations occur near the corner of the creases (see Fig. 3b), and result in undesired damage. To relieve the unnecessary buckling of facets and improve the mechanical performance of IOSs, we propose a predesign-crease strategy, i.e., setting additional creases along the diagonals of facets to guide the predictable folding rather than buckling. We sign the newly added diagonal creases as secondary creases (red lines in Fig. 3a) to distinguish from those on the side of the facets (marked as primary creases, black lines in Fig. 3a). The facet will fold along the secondary crease instead of buckling when stretching the origami spring and therefore the overwhelmed buckling is released. This strategy trades the buckling with the folding, and is named as the *origami rigidization method*. Accordingly, the abbreviated name of the IOS optimized by this method is thus updated as RIOS.

Fig. 3b shows the FEA results of the shape-morphing configurations of IOSs and RIOSs ($r_0 = 10$ mm, $n = 8$) colored by the Mises stress nephogram. One can observe that RIOSs exhibit rigidity or approximate rigidity on the facets without or with less buckling, compared to the corresponding IOS cases, especially in the square-facet cases (IOS-4 and RIOS-4). Moreover, the values of the maximal stress decrease in RIOSs compared to those in IOSs, indicating the stress concentrations are relieved.

Next, we analyze the mechanical response of IOSs and RIOSs. Fig. 3c illustrates the force-extension curves of IOSs and RIOSs. \tilde{F} is defined as $\tilde{F} = F/(2ann_{pr})$, where $2ann_{pr}$ is the total length of the primary creases with n_{pr} the number of paper ribbons. Overall, the forces required to stretch the springs follow

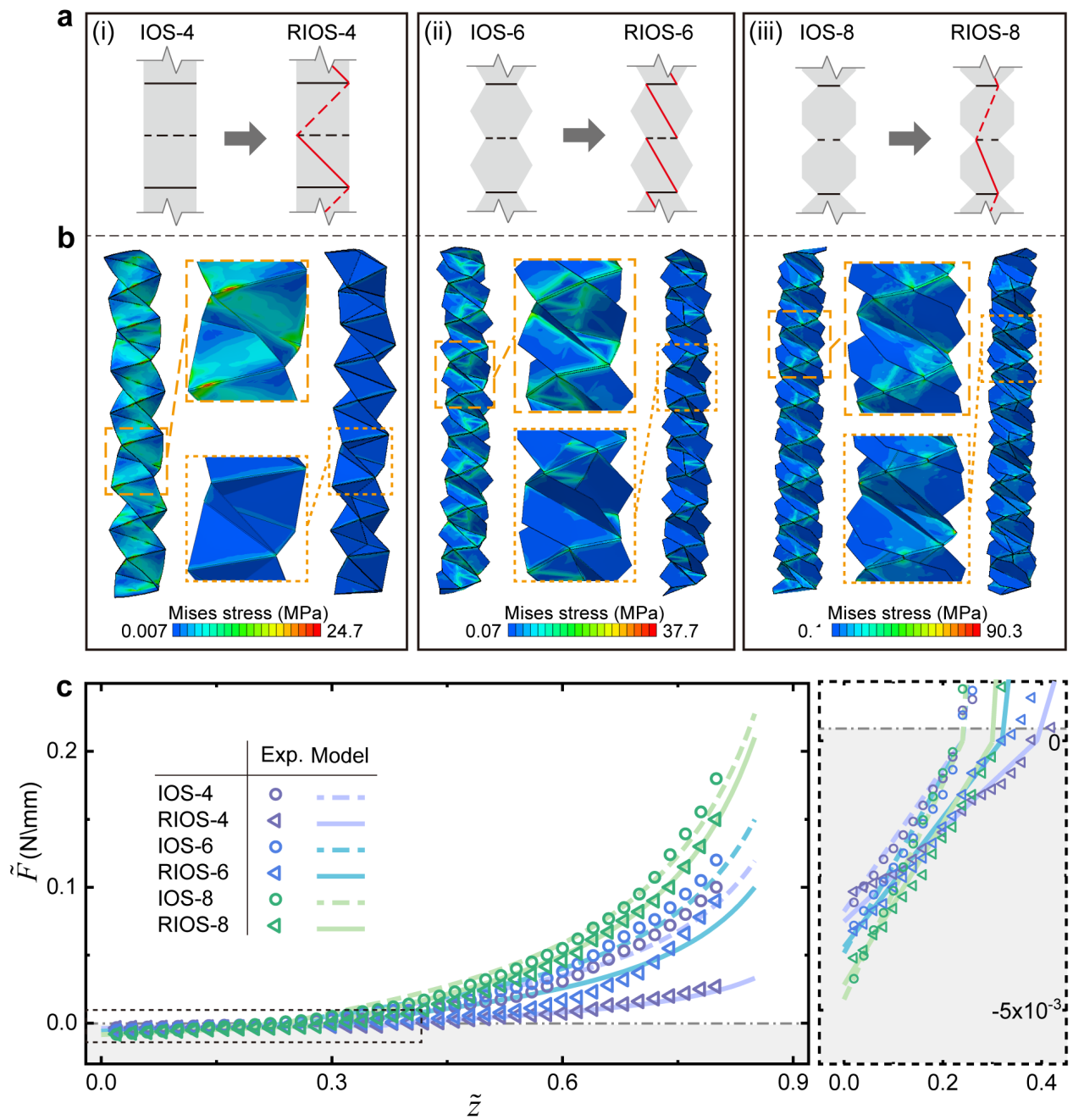


Fig. 3. Demonstration of the origami rigidization method. (a) Diagrams of the crease distributions. Black (red) lines represent primary (secondary) creases. Solid (dashed) lines are mountain (valley) creases. (b) Shape-morphing configurations ($\tilde{z} = 0.8$) obtained by FEA, colored by the Mises stress nephogram. (c) Uniaxial force \tilde{F} applied on origami springs versus extension ratio \tilde{z} . The theoretical models match the experimental data well.

IOS-4<IOS-6<IOS-8, RIOS-4<RIOS-6<RIOS-8, and RIOS<IOS under the same facet shape, while the square-facet case has the maximal difference. The force increases monotonically and continuously with respect to the uniaxial strain, which indicates no multistability or other special mechanical responses occur. Since all the origami springs exhibit an initial free extension \tilde{z}_0 due to the residual strain in creases, we separate the force-extension curves into two regions. One is the compression region, in which the origami structures are subjected to compression from their free-extension states to the minimal-length states (grey-background area in Fig. 3c); the other is the tension region, in which the origami springs are applied tension forces from the free states.

Observed from the compression region, the force and the extension of the origami springs are in an approximately linear relationship, we thus assume

$$\tilde{F} = k_c(\tilde{z} - \tilde{z}_0), \quad (6)$$

where k_c is the compression elastic constant with the unit $\text{N} \cdot \text{mm}^{-1}$ and can be obtained by linear fitting with the experimental data. As illustrated in Fig. 3c right, the regular-octagon-facet origami springs have the maximal k_c in IOS and RIOS. Moreover, RIOSs have smaller k_c than IOSs, which illustrates that the rigidization optimization on RIOSs reduces the interaction among the facets to a certain extent.

In the tension region, the force-extension relationship is no longer linear (see Fig. 3c left), which could be attributed to the stronger and stronger interactions between the adjacent facets as the extension progresses. The total shape-morphing energy E is given by the sum of the folding energy of the primary creases E_{F1} , the folding energy of the secondary creases E_{F2} ($E_{F2} = 0$ in IOSs), and the buckling energy of the facets E_B ($E_B = 0$ in RIOSs) with the forms

$$\begin{cases} E_{F1} = \frac{1}{2} \cdot f_{k_F}(\tilde{z}) \cdot 2ann_{pr} \cdot \omega_1^2, \\ E_B = \frac{1}{2} \cdot f_{k_B}(\tilde{z}) \cdot 4r_0nn_{pr} \cdot 2\omega_B^2, \\ E_{F2} = \frac{1}{2} \cdot f_{k_B}(\tilde{z}) \cdot 4r_0nn_{pr} \cdot \omega_2^2, \end{cases} \quad (7)$$

where $f_{k_F}(\tilde{z})$ and $f_{k_B}(\tilde{z})$ are the unknown stiffness of the folding creases and the buckling, respectively. Here we assume $f_{k_F}(\tilde{z}) = k_F \tilde{z}^{\xi_F}$ and $f_{k_B}(\tilde{z}) = k_B \tilde{z}^{\xi_B}$ to fit the experimental data, where k_F and k_B are the stiffness constants with the unit $\text{N} \cdot \text{mm}^{-1} \cdot \text{rad}^{-2}$, ξ_F and ξ_B are dimensionless constant exponentials in order to capture the nonlinear behavior of \tilde{F} upon \tilde{z} . The folding angle of the primary crease ω_1 can be approximately expressed as $\omega_1 = \varphi + \varphi'$ (see Supplementary Fig. 9). The buckling of the facets is simplified by two equal folding angles ω_B along the diagonals, and the folding angle of the secondary creases is denoted by ω_2 . All the folding angles are functions of \tilde{z} , obtained by evaluating coordinates (see Supplementary Information for details). We use $\tilde{E} = E/2ann_{pr}$ to denote the energy per unit length of the primary crease, therefore \tilde{F} can be expressed as the partial derivative of \tilde{E} with respect to \tilde{z} , more

specifically

$$\begin{cases} \tilde{F}_{IOS} = \frac{\partial(\tilde{E}_{F1} + \tilde{E}_B)}{\partial \tilde{z}} = \tilde{z}^{\xi_F} k_F (A_1 + A_2 \xi_F) + \tilde{z}^{\xi_B} k_B (B_1 + B_2 \xi_B), \\ \tilde{F}_{RIOS} = \frac{\partial(\tilde{E}_{F1} + \tilde{E}_{F2})}{\partial \tilde{z}} = \tilde{z}^{\xi_F} k_F (A_1 + A_2 \xi_F + C_1 + C_2 \xi_F), \end{cases} \quad (8)$$

where $A_1, A_2, B_1, B_2, C_1,$ and C_2 are the geometric correlation parameters related to \tilde{z} with expressions summarized in Supplementary Table 2. $\xi_F, \xi_B, k_F,$ and k_B are undetermined coefficients. Since $\tilde{F} = 0$ when $\tilde{z} = \tilde{z}_0$ (i.e., free states), ξ_F and ξ_B can be obtained by evaluating forces at free states. Substituting $\tilde{z} = \tilde{z}_0, \tilde{F}_{IOS} = 0$ and $\tilde{F}_{RIOS} = 0$ into Eq. (8), we have $(\xi_F)_{IOS} = -A_1(\tilde{z}_0)/A_2(\tilde{z}_0), (\xi_B)_{IOS} = -B_1(\tilde{z}_0)/B_2(\tilde{z}_0),$ and $(\xi_F)_{RIOS} = -(A_1(\tilde{z}_0) + C_1(\tilde{z}_0))/(A_2(\tilde{z}_0) + C_2(\tilde{z}_0)).$ Here we implicitly assume that the contributions from the folding term (the first term in Eq. (8)) and the bending term (the second term in Eq. (8)) to the total force in IOS are both non-negative when $\tilde{z} > \tilde{z}_0.$ Then the stiffness constants k_F and k_B can be further obtained by fitting with the experimental data using the least square method. Specific values are listed in Supplementary Table 2. Shown in Fig. 3c, the force-extension model we proposed matches well with the experimental data, indicating that the continuum mechanics models, i.e., Eq. (6) and Eq. (8), are able to accurately capture the linear and nonlinear mechanical response in the compression and tension regions.

2.4 Performance in flexible robotics.

1. Origami spring ejector. The unique shape-morphing performance of IOSs and RIOSs revealed by the previous sections implies they have potential applications in flexible robotics. Since the origami springs have excellent compressing elastic performance, it can be employed as an ejector. We arrange two ZOs in parallel with the same size and number of creases as IOS-4, named parallel origami spring (POS), to be the control group. The origami spring was firstly compressed to its minimal length by a thin sheet, and an origami hexagram was placed against the sheet. Then the elastic energy of the origami spring was released by rapidly removing the thin sheet and transformed to the kinetic energy of the origami spring and the origami hexagram for a distance ejecting. There are several factors that determine the ejecting performance of the origami springs, including the initial free extensions $z_0,$ the compression elastic constants k_c mentioned in the last section, the friction coefficient μ with the substrate, and the mass of the origami spring M and the mass of the origami hexagram m (see Supplementary Table 3 for the values of mass). By the conservation of energy, these quantities satisfy $1/2k_c z_0^2 = \mu g(mx_{ej} + Mz_0/2),$ and thus the ejecting distance

$$x_{ej} = \frac{z_0(k_c z_0 - \mu M g)}{2\mu m g}, \quad (9)$$

where g is the gravitational acceleration constant. Here, we ignore the small reciprocating motion of the origami spring for simplification. Seen from Eq. (9), it requires to increase the complete compression force of origami springs, i.e. $k_c z_0$ and decrease the mass M to obtain a good ejection ability. According to Fig. 3c, RIOSs have a relatively larger initial free extensions z_0 and smaller compression elastic constants

k_c than those in IOSs owing to the origami rigidization method. The compression force $k_c z_0$ still improves the performance to a certain extent, as shown in Fig. 4a. In conclusion, RIOSs have better ejecting ability than IOSs and POS (Fig. 4a). The RIOS-4 (Fig. 4b) shows the best performance, which can push the origami hexagram forward over three times longer than the original length of the spring.

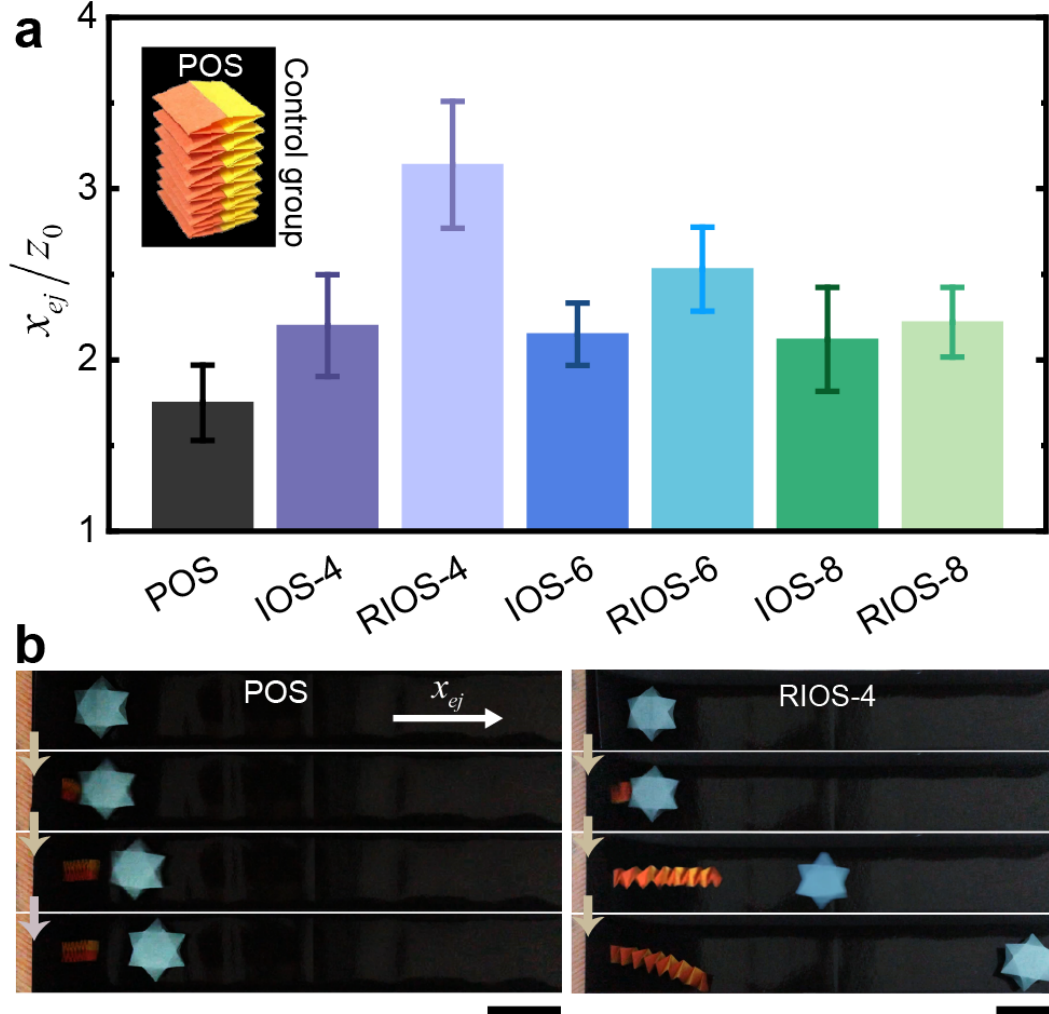


Fig. 4. Performance of origami spring ejectors. (a) The ejecting performance x_{ej}/z_0 of different origami springs. x_{ej} and z_0 are the ejecting distance of the origami hexagram and the initial length of the origami spring, respectively. (b) The ejecting process of POS and RIOS-4. All involved origami springs are under $r_0 = 10$ mm and $n = 8$. Scale bar: 50 mm.

2. *Origami spring crawler.* The origami spring crawler employs the outstanding recovery ability of the spring from its extended state to the free state. The elastic recovery performance was tested by repeatedly stretching the origami springs from their free extension states to $\tilde{z} = 0.8$, and recording the free extensions after unloading. Benefited from the mutual restraints and interactions between the paper ribbons, IOSs and RIOSs have both greatly better recovery performance than POS (Fig. 5a). Therefore, we employed the IOS-8, which had the best elastic recoverability among, to mimic the crawl locomotion of earthworms which move forward through alternately stretching and contracting the muscles along the flexible body. The two ends of the origami springs were dragged by rotary motors through two thin threads. Firstly, we

made one of the motor work to stretch the origami spring until $\tilde{z} = 0.8$. Then we stopped that motor and started the other motor to recover the stretching by relaxing the thread. The origami spring contracted to its free extension state with the head as the fixed point, and finished an entire crawling cycle (Fig. 5b).

Moreover, the origami spring crawlers have the ability to cross cliffs. Also using IOS-8 as the demonstration, the crawler can climb over a cliff step by step through properly stretching and contracting the body (Fig. 5c). When the width of the cliff increases to a considerable value, the crawler can store elastic potential energy by stretching the body, and release it instantaneously to obtain enough initial velocity to leap over the cliff like an arrow (Fig. 5d).

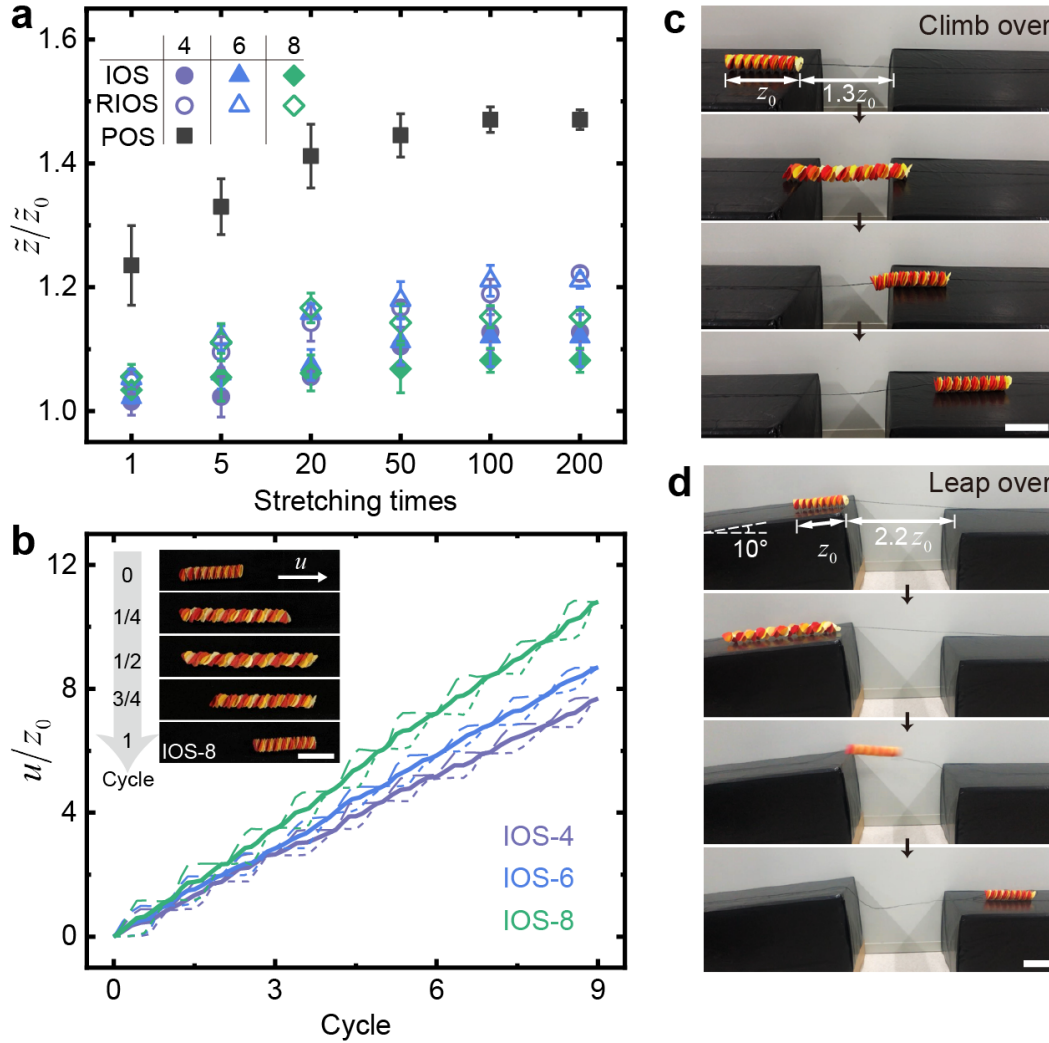


Fig. 5. Performance of origami spring crawlers. (a) The elastic recovery performance of different origami springs under multiple stretching times. (b) The crawling performance u/z_0 (u is the crawling distance) of the center of body (solid line), head (dashed line), and tail (dotted line) varying with number of crawling cycles. The thumbnail is five typical crawling moments of the IOS-8 throughout an entire crawling cycle. Crawling images of IOS-4 and IOS-6 can be seen in Supplementary Fig. 18. (c) The process of the IOS-8 climbing over a cliff with 1.3-fold body length. (d) The process of the IOS-8 leaping over a cliff with 2.2-fold body length. All involved origami springs are under $r_0 = 10$ mm and $n = 8$. Scale bar: 50 mm.

3. *Origami spring transformer.* We demonstrate an origami spring transformer utilizing the deployabil-

ity and the stretch-twist coupling. The fabrication process is exhibited in Fig. 6a, which follows three steps sequentially: connecting two IOS-4s ($r_0 = 10$ mm, $n = 4$) with opposite chirality as the shape-morphing muscle, sealing the "muscle" by thin films as the skin, and mounting two wheels on the both sides. The completed model is shown in Fig. 6b. By slowly supplying gas through the silicone tube, the origami spring transformer can transform into three configurations owing to the extensibility and flexibility of IOSs, including a closed box, an upright body, and a two-wheeled car (Fig. 6c). Furthermore, a rolling motion can be produced by employing the stretch-twist-coupling shape morphing of IOSs. As the shape morphing is symmetric with respect to the midplane, the rotation angle θ varying with the extension length z can be calculate by Eq. (4) with $\theta = 4\tilde{\theta}$ (rad) and $z = 96.4\tilde{z}$ (mm). The rolling motion is shown in Fig. 6d. The two wheels firstly got closer by removing the gas and contracting the "muscle", then the gas was rapidly supplied into the "muscle" to stretch the IOS, and the two wheels were thus pushed away. Meanwhile, the middle of the "muscle", namely the connection of the IOSs with opposite chirality underwent a twisting, and finally led the whole "car" to roll forward.

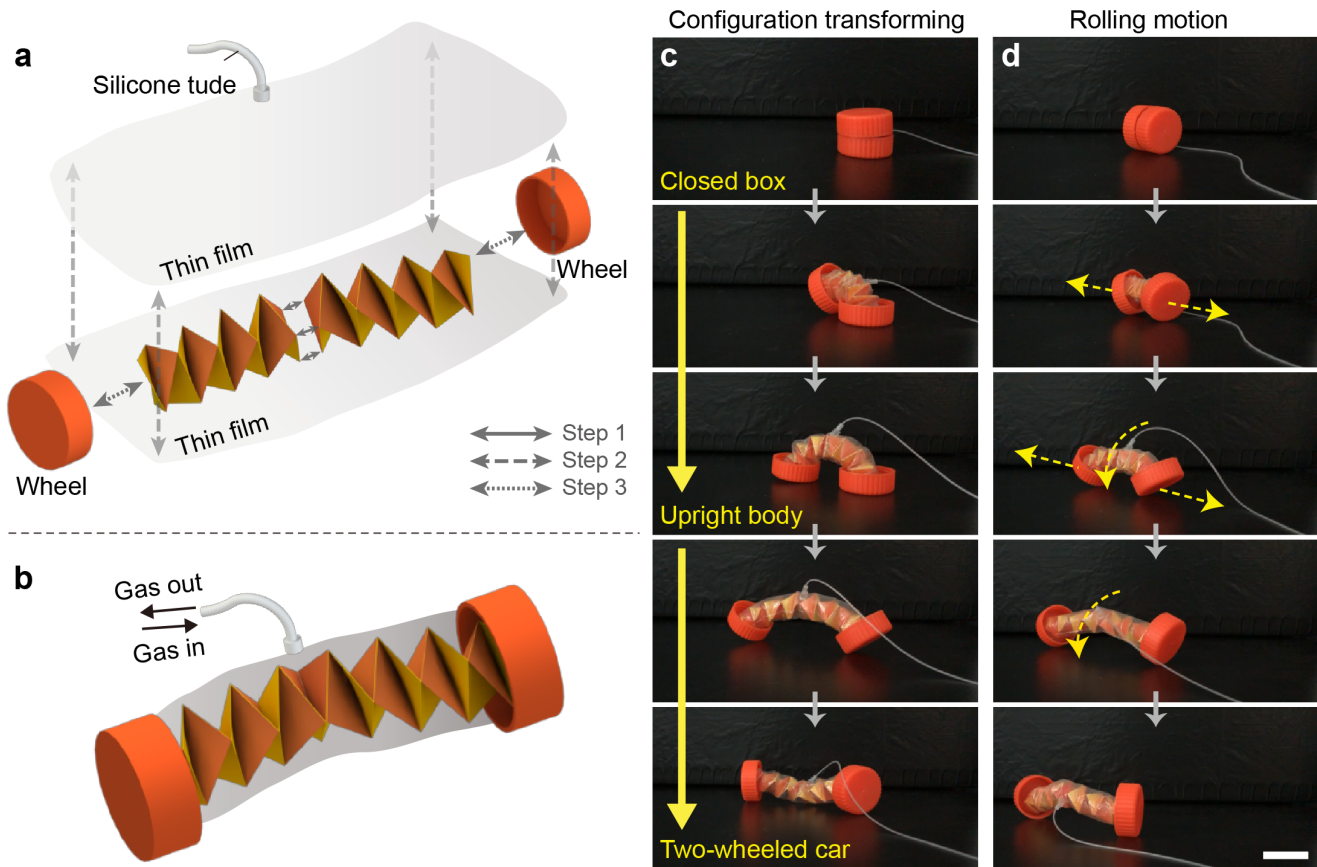


Fig. 6. Design, fabrication and resulting of an origami spring transformer. (a) The components introduction and fabrication process of the origami spring transformer. The process follows three steps, Step 1, 2, and 3 are indicated by solid-line, dashed-line, and dotted-line two-way arrows respectively. (b) The completed model. Gas is in or out via the tube to actuate the IOS. (c) The transforming process of origami spring transformer from a closed box to an upright body and then to a two-wheeled car by slowly stretching the "muscle". (d) The rolling motion of the origami spring transformer by rapidly stretching the "muscle", and utilizing the stretch-twist-coupling performance. Scale bar: 30 mm.

3 Discussion

In this work, we demonstrate that the structural design of generalized origami spring with good shape-morphing performance is of benefit to the applications of flexible robotics. We firstly present a design strategy for constructing generalized interleaved origami springs (IOS) by alternately folding multiple regular-polygon-in-chain paper ribbons under certain rules. These IOSs exhibit stretch-twist coupling under uniaxial tension due to the mutual restraints and interactions among the paper ribbons. We establish a continuum mechanics model and an origami rigidization method based on the experiments and finite element simulations to capture, analyze, and improve the shape-morphing performance of the IOSs. Guided by the theoretical framework, we propose an ejector and a crawler by employing the good elasticity of origami springs, which can push an object forward over several times longer than its initial body length, and can realize stable crawling locomotion and even cross an over-twice-body-length cliff, respectively. Moreover, we devise an origami spring transformer that is capable of three transformations (i.e., a closed box, an upright body, and a two-wheeled car) and a rolling motion by controlling the origami “muscle”.

The framework can be potentially and naturally generalized in the following ways. First, we can program the IOS using non-periodic polygon-in-chain paper ribbons so as to break the axially symmetric stretch-twist-coupling and achieve various shape-morphing performance. For example, the chain of paper ribbon can be generically curved, consisting of multiple shapes of polygon, which is expected to break the periodicity and lead to non-axial stretch-twist coupling. Alternatively, active materials such as liquid crystal elastomers can be used to design stimuli-sensitive origami springs. Moreover, compound IOSs and RIOSs have the potential to achieve programmable mechanical response. Taken together, we expect that our framework of origami-aided design will pave the way to facilitate the diverse shape morphing of flexible robotics.

4 Methods

Mechanical testing. We tested the mechanical properties of the paper for origami springs and the structures of the proposed origami springs by MTESTQuatro Testing System (ADMET, Norwood, MA). The paper for origami was cut into a dog-bone-shape standard specimen and underwent a uniaxial tension with 0.01-mm/s loading rate. We regarded the mechanical response of the paper as linear elasticity and the Young’s modulus was obtained about 1738.3 MPa after multiple measurements. IOSs and RIOSs were pulled with fine threads drawing from the midpoints of both end facets. Uniaxial tension and compression were applied both from the free extension state of each origami spring with 0.01-mm/s loading rate. The force-extension curves are exhibited in Fig. 3c.

Finite element analysis (FEA). We carried out the FEA using the commercial finite element software ABAQUS. We first set up a 3D deformable solid part of the folding zigzag origami in square (or regular hexagon, or regular octagon) facets, eight unit cells, 10-mm circumcircle radius, and 0.1-mm paper thickness. The Young’s modulus and the Poisson’s ratio were set to 1738.3 MPa and 0.3, respectively. Then the zigzag origami structures were assembled with proper relative positions to construct origami

springs. The boundaries of facets and the creases in contact were tied together to constraint their relative displacements. The center region of the bottom facet was pinned and the center region of the top facet was applied a 150-mm displacement constraint. 3D models of the origami springs were meshed using the element type C3D8R (8-node linear brick, reduced integration), while proper mesh sizes were selected to ensure the computational convergence and accuracy.

5 Acknowledgements

This work was supported by the National Natural Science Foundation of China (NSFC) under grants nos. 91848201, 11988102, 11521202, 11872004, and 11802004 and Beijing Natural Science Foundation under grants no. L172002.

6 Author contributions statement

H.D. conceived the project. Q.C. constructed and generalized the structures. Q.C. conducted the experiments and implemented the FEA simulation. Q.C. and F.F. deduced the theoretical frameworks and analysed the results of experiments, FEA, and theoretical models. Q.C., F.F., P.L., and H.D. wrote the paper. All authors discussed the results and reviewed the manuscript.

References

1. Schaffner, M. *et al.* 3D printing of robotic soft actuators with programmable bioinspired architectures. *Nat. Commun.* **9**, 878 (2018).
2. Li, S., Vogt, D. M., Rus, D. & Wood, R. J. Fluid-driven origami-inspired artificial muscles. *Proc. Natl. Acad. Sci. United States Am.* **114**, 13132–13137 (2017).
3. Hu, W., Lum, G. Z., Mastrangeli, M. & Sitti, M. Small-scale soft-bodied robot with multimodal locomotion. *Nature* **554**, 81–85 (2018).
4. Shepherd, R. F. *et al.* Multigait soft robot. *Proc. Natl. Acad. Sci. United States Am.* **108**, 20400–3 (2011).
5. Cacucciolo, V. *et al.* Stretchable pumps for soft machines. *Nature* **572**, 1–4 (2019).
6. Han, D. *et al.* Soft robotic manipulation and locomotion with a 3D printed electroactive hydrogel. *ACS Appl. Mater. & Interfaces* **10**, 17512–17518 (2018).
7. Huang, H. W., Sakar, M. S., Petruska, A. J., Pane, S. & Nelson, B. J. Soft micromachines with programmable motility and morphology. *Nat. Commun.* **7**, 12263 (2016).
8. Kotikian, A. *et al.* Untethered soft robotic matter with passive control of shape morphing and propulsion. *Sci. Robotics* **4**, eaax7044 (2019).
9. Kim, Y., Yuk, H., Zhao, R., Chester, S. A. & Zhao, X. Printing ferromagnetic domains for untethered fast-transforming soft materials. *Nature* **558**, 274–279 (2018).

10. Wang, W. *et al.* Locomotion of inchworm-inspired robot made of smart soft composite (ssc). *Bioinspiration & Biomimetics* **9**, 046006 (2014).
11. Zeng, H. *et al.* Light-fueled microscopic walkers. *Adv. Mater.* **27**, 3883–3887 (2015).
12. Zhang, X. *et al.* Optically- and thermally-responsive programmable materials based on carbon nanotube-hydrogel polymer composites. *Nano Lett.* **11**, 3239–44 (2011).
13. Plucinsky, P., Lemm, M. & Bhattacharya, K. Programming complex shapes in thin nematic elastomer and glass sheets. *Phys. Rev. E* **94**, 010701 (2016).
14. Pratapa, P. P., Liu, K. & Paulino, G. H. Geometric mechanics of origami patterns exhibiting poisson's ratio switch by breaking mountain and valley assignment. *Phys. Rev. Lett.* **122**, 155501 (2019).
15. Babaee, S. *et al.* 3D soft metamaterials with negative poisson's ratio. *Adv. Mater.* **25**, 5044–9 (2013).
16. Pan, F. *et al.* 3d pixel mechanical metamaterials. *Adv. Mater.* **31**, 1900548 (2019).
17. Waitukaitis, S., Menaut, R., Chen, B. G.-g. & Van Hecke, M. Origami multistability: From single vertices to metasheets. *Phys. Rev. Lett.* **114**, 055503 (2015).
18. Rothmund, P. *et al.* A soft, bistable valve for autonomous control of soft actuators. *Sci. Robotics* **3**, eaar7986 (2018).
19. Yang, D. *et al.* Buckling of elastomeric beams enables actuation of soft machines. *Adv. Mater.* **27**, 6323–7 (2015).
20. Rafsanjani, H., Bertoldi, K. & Studart, A. R. Programming soft robots with flexible mechanical metamaterials. *Sci. Robotics* **4**, eaav7874 (2019).
21. Felton, S., Tolley, M., Demaine, E., Rus, D. & Wood, R. A method for building self-folding machines. *Science* **345**, 644–646 (2014).
22. Yasuda, H., Tachi, T., Lee, M. & Yang, J. Origami-based tunable truss structures for non-volatile mechanical memory operation. *Nat. Commun.* **8**, 962 (2017).
23. Overvelde, J. T. *et al.* A three-dimensional actuated origami-inspired transformable metamaterial with multiple degrees of freedom. *Nat. Commun.* **7**, 10929 (2016).
24. Kamrava, S., Mousanezhad, D., Felton, S. M. & Vaziri, A. Programmable origami strings. *Adv. Mater. Technol.* **3**, 1700276 (2018).
25. Li, S., Fang, H., Sadeghi, S., Bhovad, P. & Wang, K. W. Architected origami materials: How folding creates sophisticated mechanical properties. *Adv. Mater.* **31**, e1805282 (2019).
26. Faber, J. A., Arrieta, A. F. & Studart, A. R. Bioinspired spring origami. *Science* **359**, 1386–1391 (2018).
27. Silverberg, J. L. *et al.* Origami structures with a critical transition to bistability arising from hidden degrees of freedom. *Nat. Mater.* **14**, 389–93 (2015).
28. Dang, X. *et al.* Inverse design of deployable origami structures that approximate a general surface. *arXiv: 2008.02349* (2020).

29. Yoneda, T., Matsumoto, D. & Wada, H. Structure, design, and mechanics of a paper spring. *Phys. Rev. E* **100**, 013003 (2019).
30. Filipov, E. T., Tachi, T. & Paulino, G. H. Origami tubes assembled into stiff, yet reconfigurable structures and metamaterials. *Proc. Natl. Acad. Sci.* **112**, 12321–12326 (2015).
31. Liu, J. *et al.* A novel design framework for structures/materials with enhanced mechanical performance. *Mater. (Basel)* **11** (2018).
32. Cai, J., Deng, X., Zhou, Y., Feng, J. & Tu, Y. Bistable behavior of the cylindrical origami structure with kresling pattern. *J. Mech. Des.* **137**, 061406 (2015).
33. Feng, F., Plucinsky, P. & James, R. D. Helical Miura origami. *Phys. Rev. E* **101**, 033002 (2020).

Supplementary Information

A Construction of generalized origami springs

Besides IOS-4, we also propose generalized origami springs by changing the square facets of IOS-4 into other regular-polygon shapes such as regular hexagon and regular octagon. IOS-6 is constructed by three paper ribbons consisting of a series of regular hexagons arrayed in chain. As shown in Supplementary Fig. 7, the three ribbons are placed in coincidence with the central axis 60 degrees apart, and then folded alternately in a similar way as IOS-4. IOS-8 is constructed by four paper ribbons consisting of a series of regular octagon arrayed in chain, while their central axes are 45 degrees apart, and the folded in the same way (Supplementary Fig. 8).

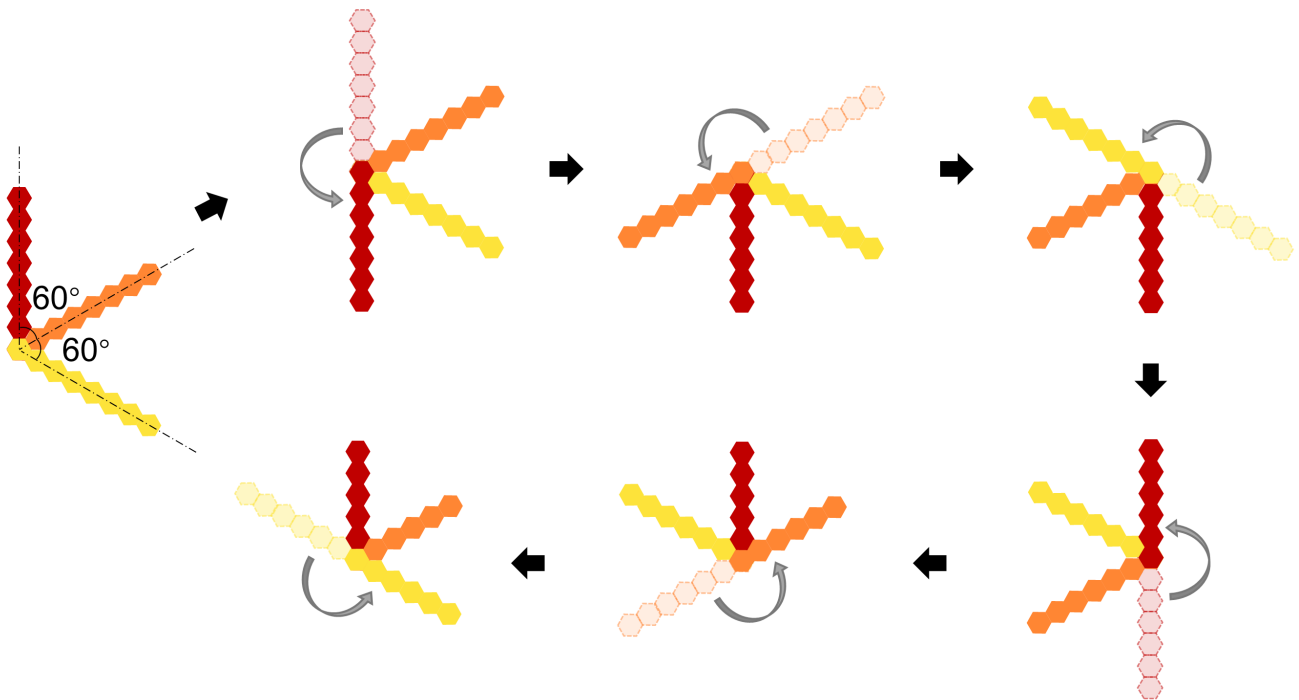


Fig. 7. Folding process of IOS-6.

B Derivations of geometrical parameters

B.1 Radius of IOS-4

Assume the edges AB , BC , CD and DA in Supplementary Fig. 9 are all straight lines with lengths a . The z -axis coordinates of the vertices on the curved surface $ABCD$ shown in Supplementary Fig. 9 can be expressed as

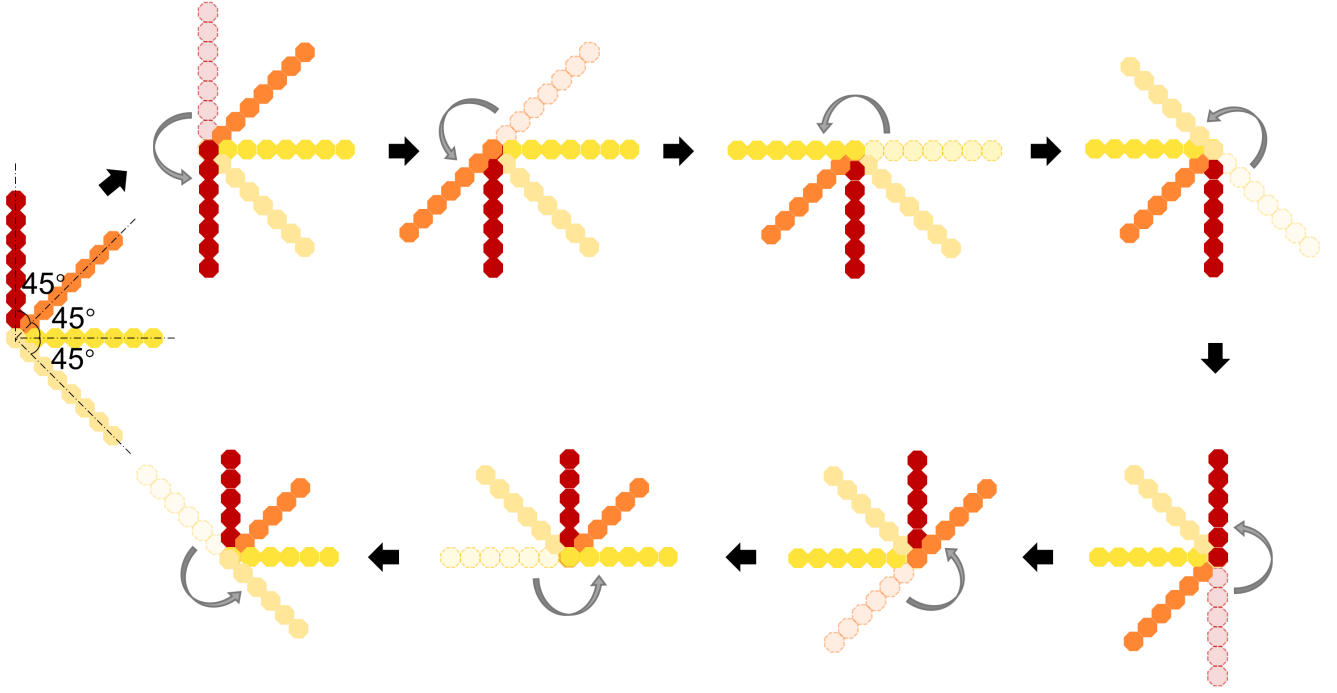


Fig. 8. Folding process of IOS-8.

$$\begin{cases} z_A = z_A, \\ z_B = z_A + a \sin \varphi, \\ z_C = z_A + \frac{2a}{3} \sin \varphi, \\ z_D = z_A + \frac{a}{3} \sin \varphi = z_A + a \sin \varphi'. \end{cases} \quad (10)$$

where φ' and φ are the helix angles of the small-pitch helix and the large-pitch helix respectively. Therefore, one can obtain the relationship between φ and φ' as

$$\varphi' = \arcsin\left(\frac{1}{3} \sin \varphi\right) = \arcsin \frac{\tilde{z}}{3}, \quad \varphi \in [0, \frac{\pi}{2}), \quad \varphi' \in [0, \arcsin \frac{1}{3}). \quad (11)$$

Further, the arc lengths of each segment on the projected circle $AB'C'D'$ (Fig. 2b in the main text) and their relations are deduced unitizing geometric analysis

$$\widehat{AB'} = r \arccos \frac{2r^2 - a^2 \cos^2 \varphi}{2r^2}, \quad (12)$$

$$\widehat{B'C'} = \widehat{C'D'} = \widehat{D'A'} = r \arccos \frac{2r^2 - a^2 \cos^2 \varphi'}{2r^2}, \quad (13)$$

$$r \arccos \frac{2r^2 - a^2 \cos^2 \varphi}{2r^2} + 3r \arccos \frac{2r^2 - a^2 \cos^2 \varphi'}{2r^2} = 2\pi r. \quad (14)$$

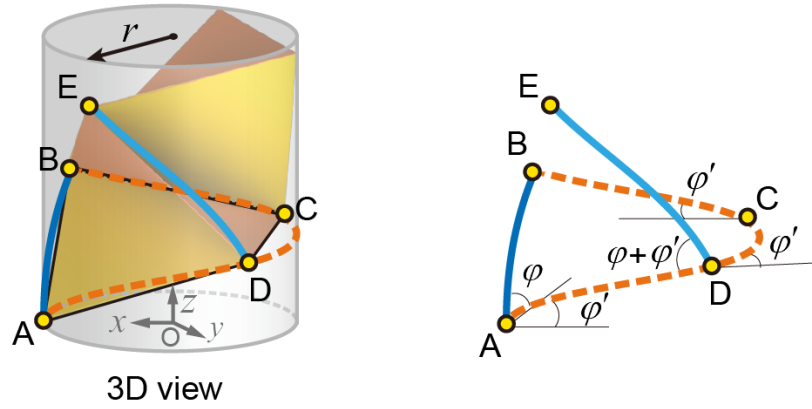


Fig. 9. Schematic of the IOS-4 unit cell. A , D , C and B are sequentially placed on the small-pitch helix with helix angle ϕ' . A and B are on the large-pitch helix with helix angle ϕ . The folding angle along the primary crease is approximated by $\phi + \phi'$, i.e., $\angle EDA$. Similar for IOS-6 and IOS-8.

Therefore, the expression of the radius r can be deduced as

$$\frac{r}{r_0} = \frac{N_4}{6} \sqrt{\frac{N_4(M_4 + N_4)}{3}}, \quad (15)$$

where $M_4 = \sqrt{1 - \tilde{z}^2}$, $N_4 = \sqrt{9 - \tilde{z}^2}$, $\tilde{z} = \sin \phi$, and $r_0 = \sqrt{2}a/2$ is the circumcircle radius of the square with side length a .

B.2 Radius of IOS-6

Similar to the derivation process of IOS-4, the z -axis coordinates of the vertices on the curved surface $ABCDEF$ shown in Supplementary Fig. 10 can be expressed as

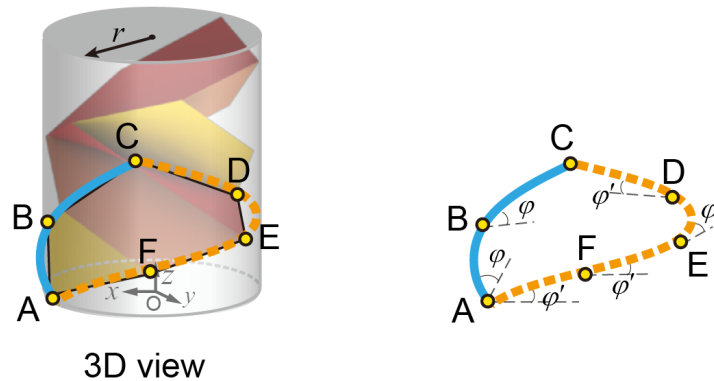


Fig. 10. Schematic of the IOS-6 unit cell. A , F , E , D and C are sequentially placed on the small-pitch helix with helix angle ϕ' . A , B and C are on one of the large-pitch helices with helix angle ϕ .

$$\begin{cases} z_A = z_A, \\ z_B = z_A + a \sin \varphi, \\ z_C = z_A + 2a \sin \varphi, \\ z_D = z_A + \frac{3a}{2} \sin \varphi, \\ z_E = z_A + a \sin \varphi, \\ z_F = z_A + \frac{a}{2} \sin \varphi = z_A + a \sin \varphi'. \end{cases} \quad (16)$$

Therefore we have

$$\varphi' = \arcsin\left(\frac{1}{2} \sin \varphi\right) = \arcsin \frac{\tilde{z}}{2}, \quad \varphi \in [0, \frac{\pi}{2}), \quad \varphi' \in [0, \arcsin \frac{1}{2}). \quad (17)$$

Further, employing the similar calculation in IOS-4, the circumference of the cylinder is expressed as

$$2\pi r = 2r \arccos \frac{2r^2 - a^2 \cos^2 \varphi}{2r^2} + 4r \arccos \frac{2r^2 - a^2 \cos^2 \varphi'}{2r^2}, \quad (18)$$

and thus

$$\frac{r}{r_0} = \frac{1}{2} \sqrt{\frac{N_6(M_6 + 2N_6) - 1}{2}}, \quad (19)$$

where $M_6 = \sqrt{3 - 3\tilde{z}^2}$, $N_6 = \sqrt{3 - \tilde{z}^2}$, and $r_0 = a$ is the circumradius of the hexagon with side length a .

B.3 Radius of IOS-8

The z -axis coordinates of the vertices on the curved surface $ABCDEFGH$ shown in Supplementary Fig. 11 can be expressed as

$$\begin{cases} z_A = z_A, \\ z_B = z_A + a \sin \varphi, \\ z_C = z_A + 2a \sin \varphi, \\ z_D = z_A + 3a \sin \varphi = z_A + 5a \sin \varphi', \\ z_E = z_A + 4a \sin \varphi', \\ z_F = z_A + 3a \sin \varphi', \\ z_G = z_A + 2a \sin \varphi', \\ z_H = z_A + a \sin \varphi'. \end{cases} \quad (20)$$

Therefore, we have

$$\varphi' = \arcsin \frac{3}{5} \sin \varphi = \arcsin \frac{3\tilde{z}}{5}, \quad \varphi \in [0, \frac{\pi}{2}), \quad \varphi' \in [0, \arcsin \frac{3}{5}). \quad (21)$$

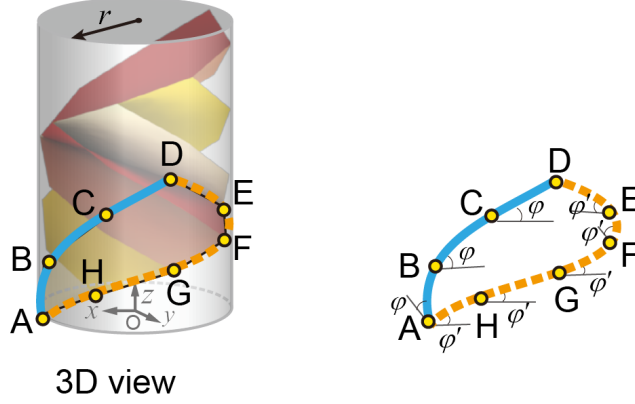


Fig. 11. Schematic of the IOS-8 unit cell. A, H, G, F, E and D are sequentially placed on the small-pitch helix with helix angle ϕ' . A, B, C and D are on one of the large-pitch helices with helix angle ϕ .

Further, by the similar calculation in IOS-4, the circumference of the cylinder is

$$2\pi r = 3r \arccos \frac{2r^2 - a^2 \cos^2 \phi}{2r^2} + 5r \arccos \frac{2r^2 - a^2 \cos^2 \phi'}{2r^2}, \quad (22)$$

and thus

$$\frac{r}{r_0} = \frac{N_8}{5} \sqrt{\frac{2(2 - \sqrt{2})}{s_{MN}}}, \quad (23)$$

where $M_8 = 5\sqrt{1 - \tilde{z}^2}$, $N_8 = \sqrt{25 - 9\tilde{z}^2}$, $s_{MN} = 5 - l_{MN}^3 - (1 + l_{MN} - l_{MN}^2)\sqrt{5 + 2l_{MN} + l_{MN}^2}$, $l_{MN} = M_8/N_8$, and $r_0 = \sqrt{1 + 1/\sqrt{2}}a$ is the circumcircle of the octagon with side length a .

The curves of r/r_0 varying with extension ratio \tilde{z} of IOS-4, IOS-6 and IOS-8 are shown in Supplementary Fig. 12, which all exhibit a decreasing trend with the increasing \tilde{z} , indicating that the radius of the cylinder decreases as the extension progresses.

B.4 Folding angles of IOS-4 and RIOS-4

The coordinates (x_i, y_i, z_i) of the vertices on the curved surface $ABCD$ shown in Fig. 2b can be expressed as

$$\begin{aligned} A(r, 0, 0), \quad B(r \cos \beta_B, r \sin \beta_B, a\tilde{z}), \\ C(r \cos \beta_C, r \sin \beta_C, \frac{2}{3}a\tilde{z}), \quad D(r \cos \beta_D, r \sin \beta_D, \frac{1}{3}a\tilde{z}), \end{aligned} \quad (24)$$

where $\beta_B = 2\pi - P_4$, $\beta_C = 2Q_4$, $\beta_D = Q_4$. See P_4 and Q_4 in Table S1 for details. The x and y coordinates are obtained by projecting the vertices onto the 2D plane perpendicular to the cylindrical axis, and the z coordinates are calculated from the helix angle and the side length. We summarize these geometrical quantities in Table 1 with no details of calculation for simplicity. Similar for IOS-6 and IOS-8. All the coordinates are functions of \tilde{z} , and therefore the geometrical quantities deduced from these coordinates are also unitary functions of \tilde{z} .

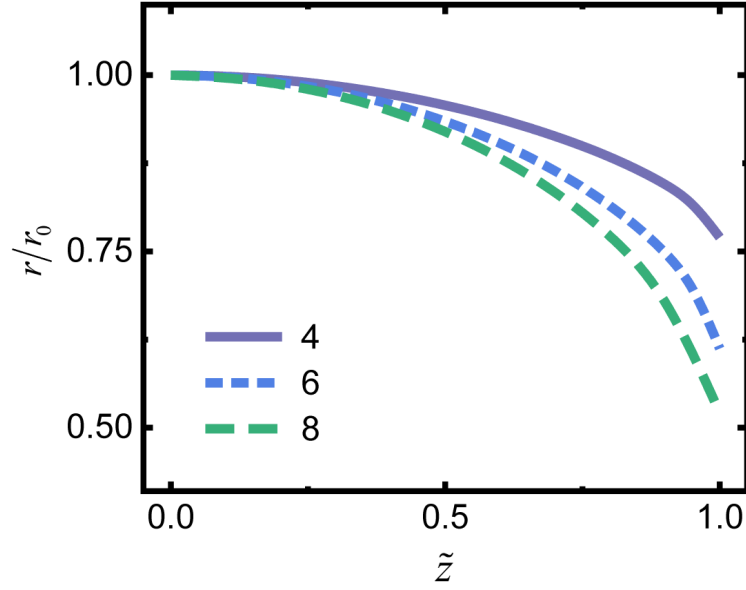


Fig. 12. r/r_0 versus the extension ratio \tilde{z} .

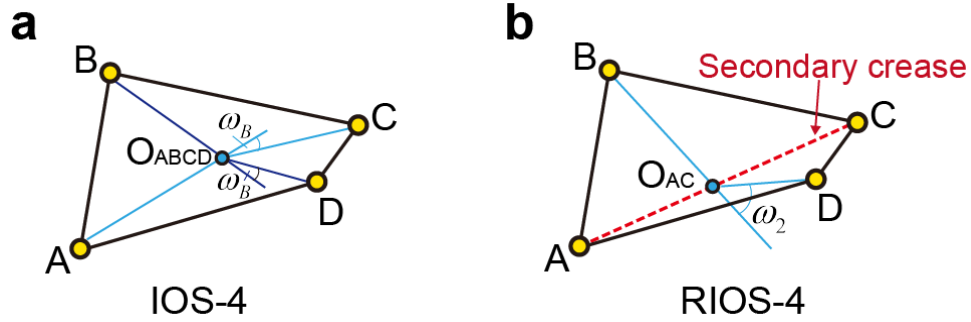


Fig. 13. Diagram of the folding angles of IOS-4 and RIOS-4. (a) ω_B of IOS-4. (b) ω_2 of RIOS-4.

We simplify the buckling of IOS-4 to two equal folding angles ω_B along the diagonal. As shown in Supplementary Fig. 13a, ω_B is calculated by

$$\omega_B = \pi - \angle AO_{ABCD}C = \pi - \angle BO_{ABCD}D, \quad (25)$$

where $O_{ABCD}((x_A + x_B + x_C + x_D)/4, (y_A + y_B + y_C + y_D)/4, (z_A + z_B + z_C + z_D)/4)$ is the center of the surface $ABCD$. ω_B is a unary function of \tilde{z} and can be deduced by coordinate evaluating.

The folding angle ω_2 along the secondary crease of RIOS-4 (Supplementary Fig. 13b) can be expressed as

$$\omega_2 = \pi - \angle BO_{AC}D, \quad (26)$$

where $O_{AC}((x_A + x_C)/2, (y_A + y_C)/2, (z_A + z_C)/2)$ is the middle point of AC . ω_2 is a unary function of \tilde{z} .

B.5 Folding angles of IOS-6 and RIOS-6

We have the coordinates of the vertices as

$$\begin{aligned} A(r, 0, 0), \quad B(r \cos \beta_B, r \sin \beta_B, a\tilde{z}), \\ C(r \cos \beta_C, r \sin \beta_C, 2a\tilde{z}), \quad D(r \cos \beta_D, r \sin \beta_D, \frac{3}{2}a\tilde{z}), \\ E(r \cos \beta_E, r \sin \beta_E, a\tilde{z}), \quad F(r \cos \beta_F, r \sin \beta_F, \frac{1}{2}a\tilde{z}), \end{aligned} \quad (27)$$

where $\beta_B = 2\pi - P_6$, $\beta_C = 4Q_6$, $\beta_D = 3Q_6$, $\beta_E = 2Q_6$, $\beta_F = Q_6$. See P_6 and Q_6 in Table S1 for detail. Therefore, the folding angle ω_B (Supplementary Fig. 14a) is deduced as

$$\omega_B = \pi - \angle AO_{ACDF}D = \pi - \angle CO_{ACDF}F, \quad (28)$$

where $O_{ACDF}((x_A + x_C + x_D + x_F)/4, (y_A + y_C + y_D + y_F)/4, (z_A + z_C + z_D + z_F)/4)$ is the center point of $ACDF$. Similarly, ω_B is a unary function of \tilde{z} .

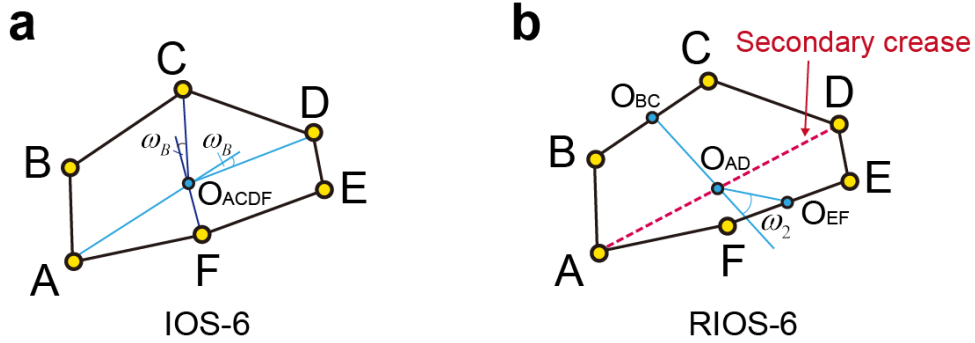


Fig. 14. Diagram of the folding angles of IOS-6 and RIOS-6. (a) ω_B of IOS-6. (b) ω_2 of RIOS-6.

The folding angle ω_2 along the secondary crease of RIOS-6 (Supplementary Fig. 14b) can be expressed as

$$\omega_2 = \pi - \angle O_{BC}O_{AD}O_{EF}, \quad (29)$$

where $O_{BC}((x_B + x_C)/2, (y_B + y_C)/2, (z_B + z_C)/2)$, $O_{AD}((x_A + x_D)/2, (y_A + y_D)/2, (z_A + z_D)/2)$, $O_{EF}((x_E + x_F)/2, (y_E + y_F)/2, (z_E + z_F)/2)$ are the middle points of CB , AD and EF respectively. Again, ω_2 is a unary function of \tilde{z} .

B.6 Folding angles of IOS-8 and RIOS-8

We have the coordinates of the vertices as

$$\begin{aligned} A(r, 0, 0), \quad B(r \cos \beta_B, r \sin \beta_B, a\tilde{z}), \\ C(r \cos \beta_C, r \sin \beta_C, 2a\tilde{z}), \quad D(r \cos \beta_D, r \sin \beta_D, 3a\tilde{z}), \\ E(r \cos \beta_E, r \sin \beta_E, \frac{12}{5}a\tilde{z}), \quad F(r \cos \beta_F, r \sin \beta_F, \frac{9}{5}a\tilde{z}), \\ G(r \cos \beta_G, r \sin \beta_G, \frac{6}{5}a\tilde{z}), \quad H(r \cos \beta_H, r \sin \beta_H, \frac{3}{5}a\tilde{z}), \end{aligned} \quad (30)$$

where $\beta_B = 2\pi - P_8$, $\beta_C = 2\pi - 2P_8$, $\beta_D = 5Q_8$, $\beta_E = 4Q_8$, $\beta_F = 3Q_8$, $\beta_G = 2Q_8$, $\beta_H = Q_8$. See P_8 and Q_8 in Table S1 for detail. Therefore, the folding angle ω_B (Supplementary Fig. 15a) is deduced as

$$\omega_B = \pi - \angle AO_{ADEH}E = \pi - \angle DO_{ADEH}H, \quad (31)$$

where $O_{ADEH}((x_A + x_D + x_E + x_H)/4, (y_A + y_D + y_E + y_H)/4, (z_A + z_D + z_E + z_H)/4)$ is the center point of $ADEH$. ω_B is a unary function of \tilde{z} .

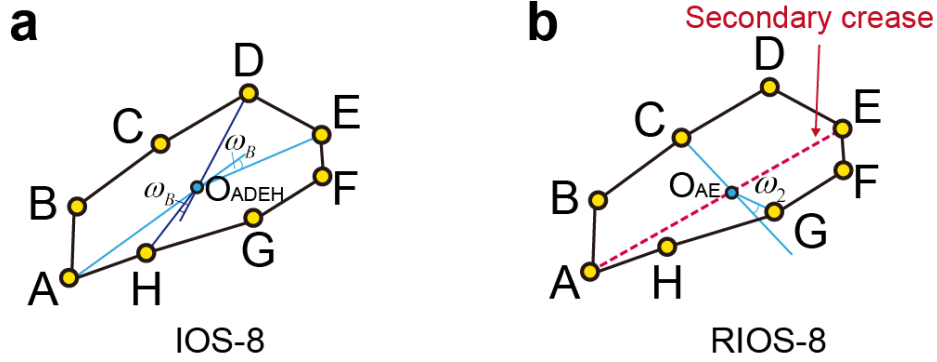


Fig. 15. Diagram of the folding angles of IOS-8 and RIOS-8. (a) ω_B of IOS-8. (b) ω_2 of RIOS-8.

The folding angle ω_2 along the secondary crease of RIOS-8 (Supplementary Fig. 15b) can be expressed as

$$\omega_2 = \pi - \angle CO_{AE}G, \quad (32)$$

where $O_{AE}((x_A + x_E)/2, (y_A + y_E)/2, (z_A + z_E)/2)$ is the middle point of AE . ω_2 is a unary function of \tilde{z} .

The curves of ω_B and ω_2 varying with extension ratio \tilde{z} of different types of origami springs are shown in Supplementary Fig. 16 and Supplementary Fig. 17, respectively, which all exhibit an increasing trend with the increasing \tilde{z} .

Table 1. Important geometric parameters of IOSs in different types.

Types	IOS-4	IOS-6	IOS-8
a	$\sqrt{2}r_0$	r_0	$\sqrt{2 - \sqrt{2}}r_0$
φ	$\arcsin \frac{z}{3}$	$\arcsin \frac{z}{2}$	$\arcsin \frac{z}{5}$
φ'	$\arcsin \frac{z}{3}$	$\arcsin \frac{z}{2}$	$\arcsin \frac{z}{5}$
$\frac{r}{r_0}$	$\frac{N_4}{6} \sqrt{\frac{N_4(M_4 + N_4)}{3}}$	$\frac{1}{2} \sqrt{\frac{N_6(M_6 + 2N_6) - 1}{2}}$	$\frac{N_8}{5} \sqrt{\frac{2(2 - \sqrt{2})}{s_{MN}}}$
$\bar{\theta}$	$4 \arccos (P_4 Q_4 + \sqrt{1 - P_4^2} \sqrt{1 - Q_4^2})$	$6 \arccos (P_6 Q_6 + \sqrt{1 - P_6^2} \sqrt{1 - Q_6^2})$	$8 \arccos (P_8 Q_8 + \sqrt{1 - P_8^2} \sqrt{1 - Q_8^2})$
l_f	$2an$	$2\sqrt{3}an$	$2(\sqrt{2} + 1)an$
λ	1.205	1.110	1.007
	$M_4 = \sqrt{1 - z^2},$ $N_4 = \sqrt{9 - z^2},$ $P_4 = 1 - \frac{108M_4^2}{N_4^3(M_4 + N_4)},$ $Q_4 = 1 - \frac{N_4(M_4 + N_4)}{12}.$	$M_6 = \sqrt{3 - 3z^2},$ $N_6 = \sqrt{3 - z^2},$ $P_6 = 1 - \frac{4M_6^2}{3N_6(M_6 + 2N_6) - 3},$ $Q_6 = 1 - \frac{N_6(M_6 + 2N_6) - 1}{N_6^2 + 1}.$	$M_8 = 5\sqrt{1 - z^2},$ $N_8 = \sqrt{25 - 9z^2},$ $P_8 = 1 - \frac{l_{MN}^2 s_{MN}}{4},$ $Q_8 = 1 - \frac{s_{MN}}{4},$ $l_{MN} = M_8/N_8,$ $s_{MN} = 5 - l_{MN}^2 -$ $(1 + l_{MN} - l_{MN}^2) \sqrt{5 + 2l_{MN} + l_{MN}^2}.$

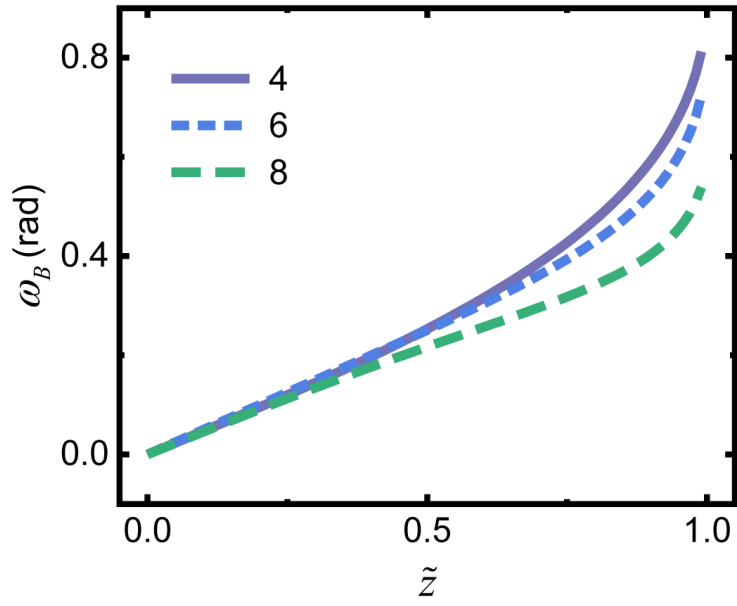


Fig. 16. ω_B versus the extension ratio \tilde{z} .

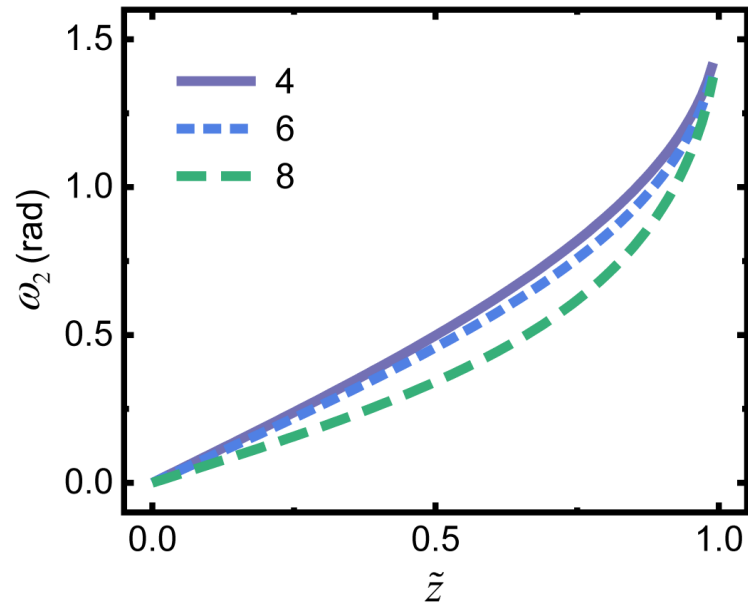


Fig. 17. ω_2 versus the extension ratio \tilde{z} .

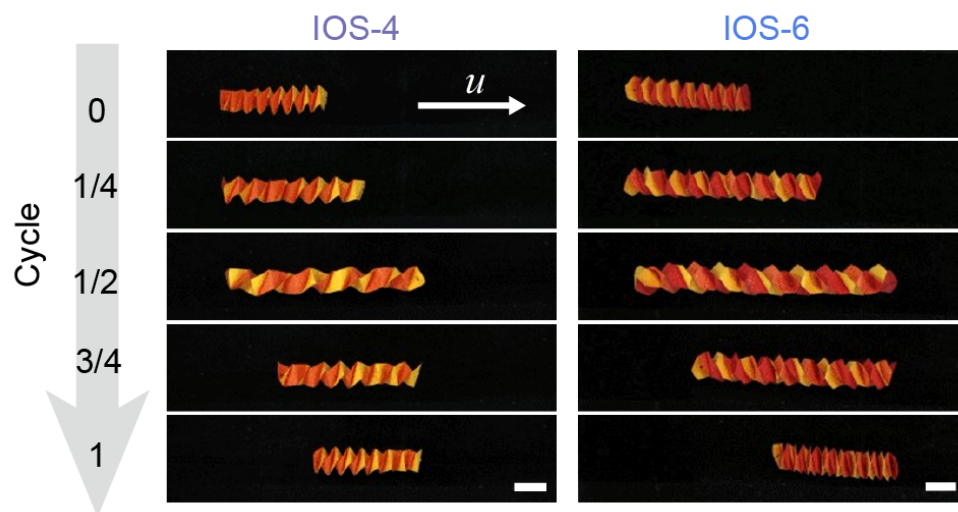


Fig. 18. Five typical crawling moments of IOS-4 and IOS-6 throughout an entire crawling cycle. Scale bar: 20 mm.

Table 2. Mechanical parameters of IOSs and RIOs in different types.

Types	IOS-4	RIOS-4	IOS-6	RIOS-6	IOS-8	RIOS-8
A_1	$(\varphi + \varphi') \frac{\partial(\varphi + \varphi')}{\partial \bar{z}}$					
A_2	$\frac{(\varphi + \varphi')^2}{2\bar{z}}$					
B_1	$2\sqrt{2}\omega_B \frac{\partial \omega_B}{\partial \bar{z}}$	-	$4\omega_B \frac{\partial \omega_B}{\partial \bar{z}}$	-	$(2^{\frac{7}{4}} + 2^{\frac{9}{4}})\omega_B \frac{\partial \omega_B}{\partial \bar{z}}$	-
B_2	$\frac{\sqrt{2}\omega_B^2}{\bar{z}}$	-	$\frac{2\omega_B^2}{\bar{z}}$	-	$(2^{\frac{3}{4}} + 2^{\frac{5}{4}}) \frac{\omega_B^2}{\bar{z}}$	-
C_1	-	$\sqrt{2}\omega_2 \frac{\partial \omega_2}{\partial \bar{z}}$	-	$2\omega_B \frac{\partial \omega_B}{\partial \bar{z}}$	-	$(2^{\frac{3}{4}} + 2^{\frac{4}{4}})\omega_2 \frac{\partial \omega_2}{\partial \bar{z}}$
C_2	-	$\frac{\sqrt{2}\omega_2^2}{2\bar{z}}$	-	$\frac{\omega_2^2}{\bar{z}}$	-	$(2^{-\frac{1}{4}} + 2^{\frac{1}{4}}) \frac{\omega_B^2}{\bar{z}}$
\tilde{z}_0	0.242	0.385	0.241	0.319	0.239	0.302
ξ_F	-2.031	-2.110	-2.030	-2.081	-2.030	-2.080
ξ_B	-2.062	-	-1.997	-	-1.942	-
k_c (N·mm ⁻¹)	0.013	0.009	0.016	0.012	0.020	0.015
k_F (N·mm ⁻¹ , rad ⁻²)	0.060	0.012	0.076	0.028	0.123	0.029
k_B (N·mm ⁻¹ , rad ⁻²)	0.040	-	0.040	-	0.040	-

Table 3. Mass of the involved origami structures.

Types	Mass (g)
IOS-4 & RIOS-4	0.398
IOS-6 & RIOS-6	0.795
IOS-8 & RIOS-8	1.075
POS	0.198
Origami hexagram	0.362